applied optics

Reconstruction of laser-induced cavitation bubble dynamics based on a Fresnel propagation approach

Luis Felipe Devia-Cruz,[1,*] Santiago Camacho-López,[1] Víctor Ruiz Cortés,[1] Victoria Ramos-Muñiz,[1] Francisco G. Pérez-Gutiérrez,[2] and Guillermo Aguilar[3]

[1]Departamento de Óptica, Centro de Investigación Científica y de Educación Superior de Ensenada, Ensenada, 22860 BC, Mexico
[2]Facultad de Ingeniería, Universidad Autónoma de San Luis Potosí, 78290 San Luis Potosí, SLP, Mexico
[3]Department of Mechanical Engineering, University of California, Riverside, Riverside, California 92521, USA
*Corresponding author: lfdevia7@gmail.com

Received 10 August 2015; revised 7 November 2015; accepted 12 November 2015; posted 13 November 2015 (Doc. ID 247589); published 9 December 2015

A single laser-induced cavitation bubble in transparent liquids has been studied through a variety of experimental techniques. High-speed video with varying frame rate up to 20×10^7 fps is the most suitable to study nonsymmetric bubbles. However, it is still expensive for most researchers and more affordable (lower) frame rates are not enough to completely reproduce bubble dynamics. This paper focuses on combining the spatial transmittance modulation (STM) technique, a single shot cavitation bubble and a very simple and inexpensive experimental technique, based on Fresnel approximation propagation theory, to reproduce a laser-induced cavitation spatial dynamics. Our results show that the proposed methodology reproduces a laser-induced cavitation event much more accurately than 75,000 fps video recording. In conclusion, we propose a novel methodology to reproduce laser-induced cavitation events that combine the STM technique with Fresnel propagation approximation theory that properly reproduces a laser-induced cavitation event including a very precise identification of the first, second, and third collapses of the cavitation bubble.

OCIS codes: (050.1960) Diffraction theory; (070.0070) Fourier optics and signal processing; (350.3390) Laser materials processing.

http://dx.doi.org/10.1364/AO.54.010432

1. INTRODUCTION

Laser induced cavitation (LIC) is a fast and complex phenomenon which has been studied from a variety of perspectives in order to develop new potential applications. Laser cavitation dynamics in liquids integrates several processes such as photodisruption, shockwaves generation, bubble growth and collapse, rebounding bubbles, sonoluminescence [1], and high-speed liquid jets formation [2]. Its use in medicine has led several studies about cavitation-tissue interactions, i.e., cell damage [3], tissue cutting [4,5], biomaterial remotion [5], and lithotripsy [6]. The LIC phenomenon starts after a dielectric breakdown, which is defined as a fast material ionization, it occurs when a substance that is a poor conductor of electricity is strongly ionized by absorption of electromagnetic energy [7]. This physical mechanism for bubble generation is reviewed in [8] and references therein.

The growth, collapse, oscillating behavior of the cavitation bubbles, jet formation, and luminescence have been studied using different techniques, e.g., time-resolved shadowgraphy (TRS) [9,10], photomultiplier tubes [11], Schlieren photography [12], high-speed photography [9,13], streak camera imaging (SCI) [10,14], interferometry [15], and beam deflection probe (BDP) [16,17], among others. Recently, the spatial transmittance modulation (STM) technique was reported [18] for the study of LIC phenomenon, this technique delivers a fast photodiode electric trace that contains the whole bubble dynamics in a single shot, including bubble growth, collapse, and subsequent growth and collapses.

Table 1 shows a classification of LIC characterization techniques, taking into account the data acquisition method and number of cavitation events required to retrieve the whole bubble dynamics. The disadvantage of imaging techniques, such as TRS and SCI, is that they require time-consuming image processing; those techniques are suitable for monitoring irregular LIC dynamics. The disadvantage of methods that require multiple bubbles, like TRS and BDP, is that each LIC event fluctuates from shot to shot [19]; therefore, reconstruction of the LIC dynamics through these methods produces only an average over many similar events. As an advantage, the STM technique produces a fully characterized LIC event on a single laser shot in a very fast manner, and with precision as high as

Table 1. Classification of LIC Characterization Techniques, Taking into Account the Data Acquisition Method and the Number of Cavitation Events Required

Data Acquisition Through	Required Number of Laser-Induced Cavitation Bubbles for Full Dynamics Characterization	
	Multiple Bubbles	Single Bubble
Image processing (Long processing time)	Time-resolved shadowgraphy (TRS)	Streak camera imaging (SCI)[a]
Electrical trace processing (Short processing time, requires stand still bubble position)	Beam deflection probe (BDP)	*Spatial transmittance modulation (STM)*[a]

[a]Only for symmetrical bubbles.

the sampling rate of the oscilloscope used (1×10^7 samples per second in our case). The latter is particularly important in respect to capturing the exact bubble collapse time. A limitation of the STM technique is that the bubble must be smaller than the probe beam and is useful for symmetric bubbles only.

The present paper focuses on taking advantage of the STM intensity signal, i.e., the electrical trace in order to calculate the bubble radius evolution on time $r(t)$ using the Fresnel approach. The main advantage of this novel method is its experimental simplicity and low cost to reproduce LIC dynamics at 1×10^7 samples per second, which is fast enough to resolve LIC events much better and with superior features to what it can be achieved through video at 75,000 fps. Brujan et. al. [9] used video recording at 20×10^7 fps to observe the collapse of an ultrasound-driven bubble cloud near a solid boundary. While video at 20×10^7 fps has a better time resolution to study bubble cloud collapse than that of the STM technique, its high cost is prohibitive for most researchers. It is pointed out here that the time resolution of our technique can be easily increased up to 1×10^9 samples per second with an appropriate oscilloscope setting and photodetector capabilities.

2. MATERIALS AND METHODS

A. Experimental Setup

Figure 1 shows the experimental setup used to monitor plasma mediated cavitation bubble dynamics. It combines the STM technique and a high-speed video system [18,20]. Bubbles were produced by the pump laser, a Q-switched, 532 nm (frequency doubled), Nd:YAG, running at 10 Hz repetition rate with energy per pulse up to 820 μJ ± 57 μJ. The probe beam for the STM technique was provided by a 632.8 nm, 0.5 mW, continuous wave, He–Ne laser.

These two beams were brought collinearly to a glass cuvette, containing distilled water, by means of a dichroic mirror; the combination of lenses L1 ($f = 100$ mm) and L2 ($f = 25.4$ mm) allowed to focus the pump pulse within the water, while the probe beam passed collimated through the cuvette with a 1150 μm diameter (FWHM). A third lens L3 ($f = 75$ mm) focused the probe beam onto a 1 ns rise time photodiode, while a long-pass

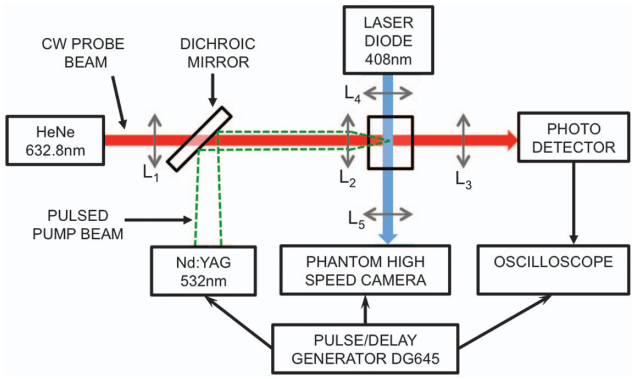

Fig. 1. Experimental setup for simultaneous STM technique and high-speed video recording.

filter positioned in front of the photodiode blocked out the transmitted light from the pump pulse.

High-speed video frames were acquired orthogonally to the pump-probe propagation direction using a Phantom MIRO M/LC310 camera at 75,000 fps. A 408 nm, 4 mW laser diode provided the illumination for the video; the image was formed using lenses L4 ($f = 200$ mm) and L5 ($f = 7$ mm).

In our experiments both techniques, the STM and high-speed video, were run simultaneously. For that aim, the pump laser Q-switch external trigger was synchronized to both the camera and the oscilloscope using an electronic trigger delay/pulse generator (DG645; M/s Stanford Research Systems).

B. Bubble Radius Estimations from the Fresnel Approximation Analysis

Figure 2(a) depicts the optical path of the collimated probe beam (HeNe at 632.8 nm) through three optical planes (bubble, lens and photodiode) that affect the STM probe beam propagation.

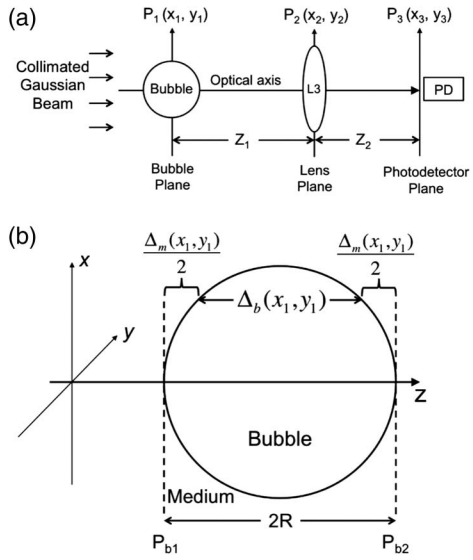

Fig. 2. (a) Gaussian probe beam propagation path between the bubble plane P_1 and the STM photodiode plane P_3. (b) Side view of the optical thickness for the bubble and the surrounding medium between the bubble planes P_{b1} and P_{b2}.

In order to numerically calculate the intensity measured by the photodiode at plane P_3, we first obtained the field distribution at the plane P_2, that is, the diffracted field due to the bubble, and then the field distribution at the plane P_3, where the lens L3 had focused the diffracted field obtained at P_2. Both field distributions were calculated using the Fresnel Approximation Diffraction Integral (FDI) [21] starting at plane P_1. In consequence, a theoretical STM trace corresponding to the intensity at the photodiode plane P_3 was computed by integrating the intensity distribution at the plane P_3.

The incident plane wave with a Gaussian amplitude profile illuminating the bubble is given by Eq. (1):

$$E_{\text{inc}}(x_1, y_1) = E \exp\left(-\frac{x_1^2 + y_1^2}{w^2}\right), \tag{1}$$

where E_{inc} is the incident electric field, and w is the beam waist size. The bubble introduces a phase delay into the incident wave front proportional to the optical path, we consider that the index of refraction inside the bubble is isotropic.

Let the thickness of the bubble at any given position (x_1, y_1) be $\Delta_b(x_1, y_1)$ and $\Delta_m(x_1, y_1)$ the thickness of the remaining medium between the two planes P_{b1} and P_{b2} inside the bubble aperture, see Fig. 2(b). We consider the observation distance, that is z_1 (distance from the plane P_1 to the plane P_2), to be much larger than the wavelength. This consideration is necessary according to Goodman [21]. Our experiment setup always fulfilled the condition to apply the Fresnel Approximation Diffraction Integral. Thus, the total phase delays introduced to the incident plane wave are given by Eq. (2). This relation includes the refractive indexes of water (1.35) and water vapor (1.000087 at 500°C). Both refractive index values were calculated for 1 atm, external pressure and $\lambda = 589$ nm, according to Schiebener *et al.* [22]:

$$\phi(x_1, y_1) = \begin{cases} kn_m(2R) & \sqrt{x_1^2 + y_1^2} > R \\ kn_m\Delta_m(x_1, y_1) + kn_b\Delta_b(x_1, y_1) & \sqrt{x_1^2 + y_1^2} \le R \end{cases}, \tag{2}$$

where n_m and n_b are the refractive index of the medium and the bubble, respectively, ϕ is the phase shift in terms of the optical path, k is the wave number, and R is the radius of the bubble. We can also write the effect of the bubble on the phase front of the probe beam as a multiplicative phase term given by φ_b in Eq. (3):

$$\varphi_b(x_1, y_1) = \exp[i\phi(x_1, y_1)]. \tag{3}$$

Then, the product of the complex amplitude directly in front of the bubble and the phase transformation φ_b, produces the complex amplitude E_b right after the bubble, given by Eq. (4):

$$E_b(x_1, y_1) = \varphi_b(x_1, y_1)E_{\text{inc}}(x_1, y_1). \tag{4}$$

The mathematical forms of the thickness functions are given by Eqs. (5) and (6):

$$\Delta_b(x_1, y_1) = 2\sqrt{R^2 - (x_i^2 + y_i^2)}, \tag{5}$$

$$\Delta_m(x_1, y_1) = 2\left[R - \sqrt{R^2 - (x_i^2 + y_i^2)}\right]. \tag{6}$$

To find the complex amplitude distribution at the plane P_2, we applied the FDI as Eq. (7):

$$E(x_2, y_2) = \frac{e^{ikz_1}}{i\lambda z_1} e^{i\frac{k}{2z_1}(x_2^2 + y_2^2)} \int_{-\infty}^{\infty}\int_{-\infty}^{\infty}\left\{E_b(x_1, y_1)e^{i\frac{k}{2z_1}(x_1^2 + y_1^2)}\right\} e^{-i\frac{2\pi}{\lambda z_1}(x_1x_2 + y_1y_2)}\,dx_1\,dy_1. \tag{7}$$

To numerically calculate the complex amplitude at any given point, we interpreted Eq. (7) as the Fourier Transform of the complex field right after the bubble, multiplied by a phase factor and evaluated at the spatial frequencies $f_x = x_2/\lambda z_1$ and $f_y = y_2/\lambda z_1$, then we can rewrite the Eq. (7) as Eq (8):

$$E(x_2, y_2) = \frac{e^{ikz_1}}{i\lambda z_1} e^{i\frac{k}{2z_1}(x_2^2 + y_2^2)} F\left\{E_b(x_1, y_1)e^{i\frac{k}{2z_1}(x_1^2 + y_1^2)}\right\}\Big|_{\substack{f_x = x_2/\lambda z_1 \\ f_y = y_2/\lambda z_1}}. \tag{8}$$

Now the amplitude distribution E' at the plane P_2 just after the lens L_3 is given by Eq. (9):

$$E'(x_2, y_2) = E(x_2, y_2)P(x_2, y_2)e^{-i\frac{k}{2f}(x_2^2 + y_2^2)}, \tag{9}$$

where $P(x, y)$ is associated with the lens pupil function $P(x, y)$ defined by Eq. (10):

$$P(x, y) = \begin{cases} 1 & \text{inside the lens aperture} \\ 0 & \text{otherwise} \end{cases}. \tag{10}$$

Determination of the bubble radius as a function of time involves the development of a computational algorithm based on the theory described in Eqs. (1)–(10) to calculate the complex amplitude at planes P_2 and P_3 combined with the normalized experimentally obtained STM signal. The inputs for the algorithm were propagation distances (z_1 and z_2), the probe laser wavelength (λ), the probe beam size (w), the focal distance of lens L3 (f), a proposed bubble radius increment (ΔR), time step (Δt), and experimentally acquired STM signal data, as described in the flow chart of Fig. 3.

Integration of the complex amplitude at plane P_3 represents the light intensity that reaches the photodetector, which is maximum at $t = 0$ when there is no bubble, and decreases when some bubble radius is introduced. The theoretical intensity at the photodetector when there is no bubble is referred to as I_0. For a time t_1 with a specified time step Δt, the algorithm proposes a bubble radius R_1 and integrates the light intensity that reaches the photodetector; the result of such integration divided by I_0 is the I_1 value; such theoretical I_1 value is compared against the corresponding intensity value of the experimentally obtained STM signal at $t = t_1$. If the integrated intensity is larger than the experimentally obtained, a larger R_1 value is proposed until both the theoretically integrated and the experimentally obtained intensities match. The process is continuously repeated for a new time t_2 and so on until a plot of calculated bubble radius as a function of time $R(t)$ is obtained.

The effect of the water vapor refractive index values at temperatures ranging between 100 and 500°C was verified. It was found that because the difference in refractive index value between 100 and 500°C is 0.000101, it does not affect the final result of the simulation. A comparison between the reproduction of bubble dynamics using refractive index values of water

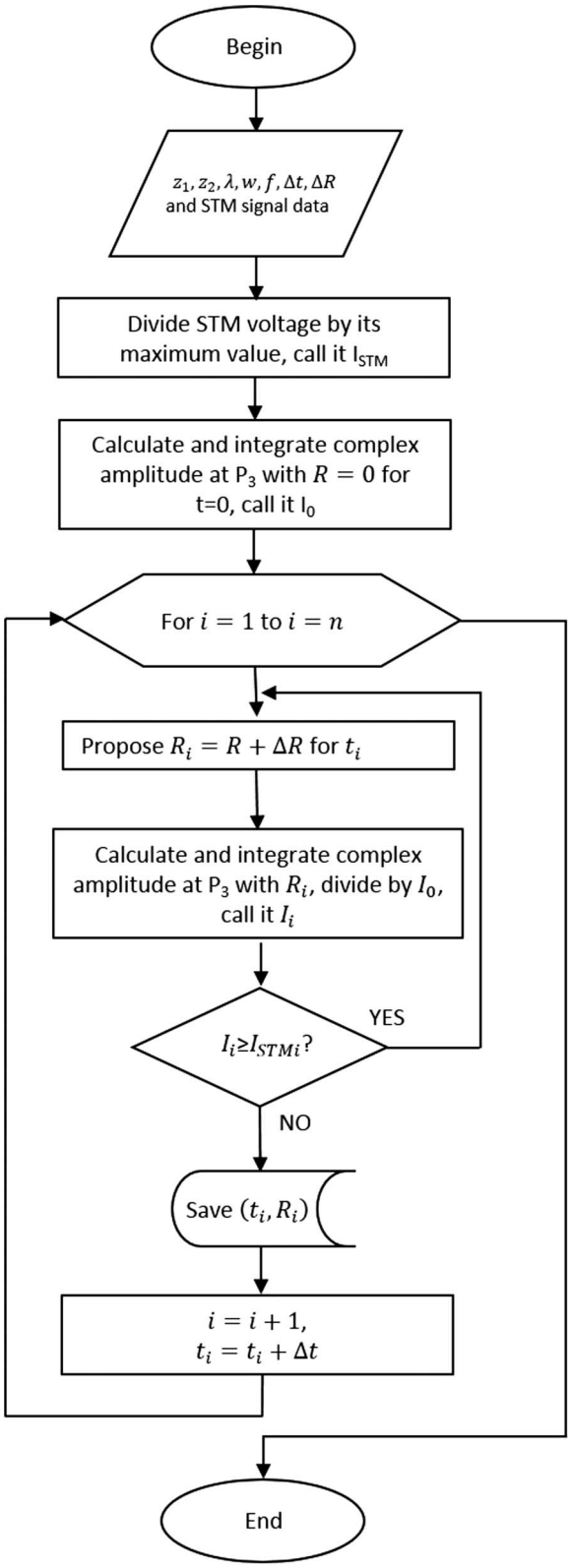

Fig. 3. Data flow chart for the theoretical calculation of bubble dynamics.

vapor at 100 and 500°C is shown in Fig. 4. Laser pulse energy in this figure is 1800 μJ. As this figure serves for demonstration purposes only, it displays one out of 16 data points that our code simulates based on the information provided by the STM oscilloscope trace.

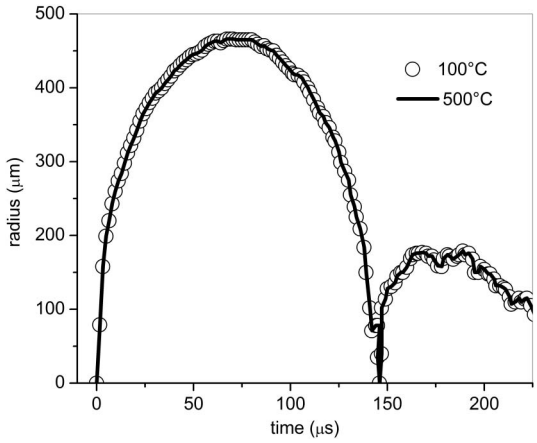

Fig. 4. Comparison of laser induced cavitation bubble dynamics using refractive index values of water vapor at 100 and 500°C. Laser pulse energy for this experiment was 1800 μJ, which corresponds to 1.02×10^6 mJ/cm^2 laser fluence.

3. RESULTS AND DISCUSSION

Figures 5(a)–5(c) show the intensity distribution calculated from the complex amplitudes just before the lens (L3); it was possible to observe a pattern of light that looks very similar to some of the experimental shadowgraph features [Fig. 5(d)], for instance, the light that is transmitted through the bubble center which is not deviated as the rest of the light beam. We could refer to these plots as *theoretical shadowgraphs*.

In the shadowgraphy experiments the central portion of the wavefront (of the probe beam) crosses two interfaces at normal incidence: (a) water to gas and (b) gas to water. For a small cross

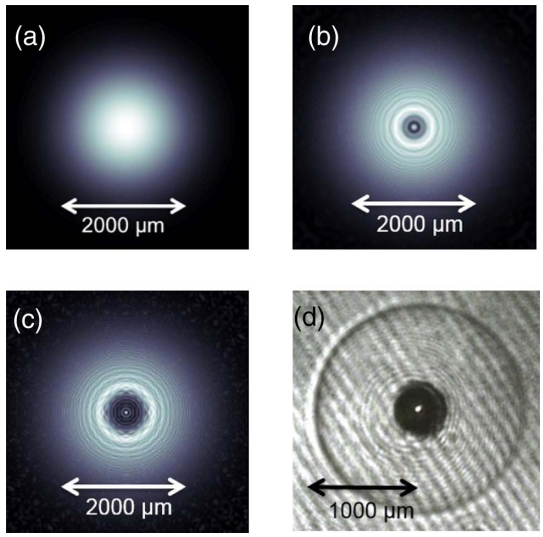

Fig. 5. Frames (a), (b), and (c) correspond to theoretical shadowgraphs obtained by plotting the intensity calculated from the complex amplitude at the plane $P_2(x_2, y_2)$; (d) experimental time resolved shadowgraph of bubble and shockwave, taken 50 μs after the plasma formation.

section as compared to the bubble surface, these interfaces could be assumed as quasi-flat interfaces, so that the laser beam is normally incident, which allows the light to pass through the bubble without being refracted; therefore, for any bubble size there is always a light spot right at the bubble center; this feature is reproduced in the theoretical shadowgraphs just as it appears also in our experimental laser pump-probe shadowgraphs [20,23] [Fig. 5(d)].

During the experimental data collection, the oscilloscope traces and the high-speed video images were saved together for later frame-by-frame analysis, providing insight of the bubble dynamics phenomenon all in a single shot. Figure 6 shows the correspondence between the STM signal (black solid line) and measured radii with the high speed camera (blue circles); it must be noticed that the 75,000 fps video was not able to detect the exact instant of the bubble collapses, it missed the first, second, and the third collapses, while the STM trace shows this very clearly and precisely.

The complementary computational algorithm based on the FDI propagation theory properly reproduces the laser-induced cavitation event; it makes it possible to determine the bubble radius dynamics preserving the STM trace time resolution, about 1×10^7 samples per second. A direct comparison between experimentally measured bubble radius (blue circles) taken from the high-speed (75,000 fps) bubble shadowgraphs, and the numerically computed bubble radius (red dashed line), which are based on the experimental STM trace, shows very good agreement. The slight deviation from the experimental data points might be explained by the fact that the bubble growth/collapse process is rather complex and includes: a very small size in the beginning (favors diffraction effects), a hot plasma and unstable gas and vapor (favors scattering); later an inhomogeneous mixture of "noncondensable" gases and vapor [6] give place to a inhomogeneous refractive index across the bubble. Even when the inner gas mixture pressure is assumed to

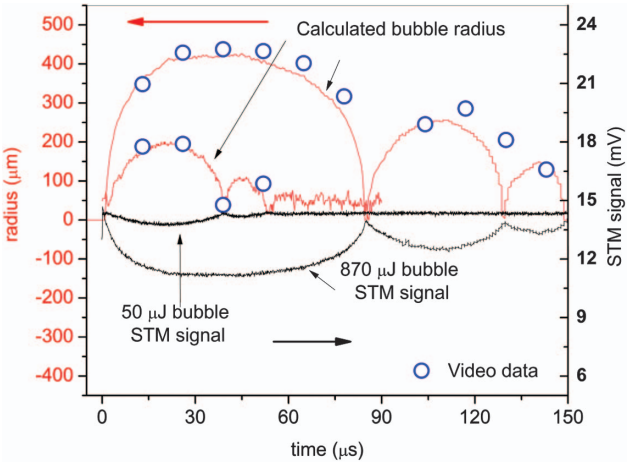

Fig. 6. Solid black trace corresponds to the experimental intensity related electric STM signal. At the maximum bubble size, most incident light is diffracted, refracted, or scattered out of the photodiode, and corresponds to a minimum of the measured intensity. The upper solid red line corresponds to the calculated bubble radius. The blue circles are experimentally measured bubble radii from the high-speed video. The 50 and 870 μJ laser pulse energies correspond to a 2.8×10^4 and 4.9×10^5 mJ/cm^2 laser fluence, respectively.

be uniform, the inner gases temperature and density distribution are not [24]. Thus, the bubble index of refraction that depends on the temperature and density distribution is nonuniform. Therefore, it is quite remarkable that even considering a homogeneous refractive index for the FDI computation in our model, it reproduces the bubble evolution both in space and time very close to the one experimentally measured.

4. CONCLUSIONS

A novel analysis of the laser-induced cavitation phenomenon is presented in this paper, which contributes to the field of cavitation by adding knowledge to the current characterization techniques. The analysis presented here allows for reproducing the whole dynamics of a symmetric cavitation bubble event. It provides the bubble size as a function of time, and the first, second, and third collapse times through a very simple and inexpensive experimental method combined with the FDI theory.

Having a reliable method to determine the bubble size and the precise collapse times is very relevant since these two quantities are related to some of the system parameters, for instance, the maximum radius of the bubble or the collapse time are closely related to the bulk water pressure. Therefore, by knowing the bubble evolution accurately, one can estimate some unknown parameters of the system, which may be the case for some cavitation applications in medicine or biophotonics.

We must point out that working our FDI approach under the assumption that the refractive index is uniform for both the bubble content and the surrounding water is far from the real refractive index for those two regions. Instead, the refractive index of water surrounding the bubble depends on density and temperature [22]; both water parameters are affected by the bubble wall displacement and by the thermal energy exchange with the bubble contents. The refractive index within the bubble also varies with time mainly due to the changes of pressure and temperature. Therefore, it would be our next goal to develop a good method to dynamically estimate the actual refractive index of water in the close proximity to the bubble wall and also the refractive index within the bubble. These would improve our Fresnel propagation approach prediction of the cavitation bubble dynamics.

Funding. Conacyt (205911, 245776).

Acknowledgment. The authors acknowledge partial support to this research work by Oftálmica Internacional.

REFERENCES

1. C.-D. Ohl, T. Kurz, R. Geisler, O. Lindau, and W. Lauterborn, "Bubble dynamics, shock waves and sonoluminescence," Philos. Trans. R. Soc. London, Ser. A **357**, 269–294 (1999).
2. T. Tominaga, A. Nakagawa, T. Hirano, J. Sato, K. Kato, and S. H. R. Hosseini, "Application of underwater shock wave and laser-induced liquid jet to neurosurgery," Shock Waves **15**, 55–67 (2006).
3. D. Lapotko and E. Lukianova, "Laser-induced micro-bubbles in cells," Int. J. Heat Mass Transfer **48**, 227–234 (2005).
4. T. Juhasz, R. Kurtz, F. Raksi, C. Suarez, C. Horvath, and G. Spooner, "The femtosecond blade: Applications in corneal surgery," Opt. Photon. News **13**(1), 24–29 (2002).

5. T. Juhasz, F. H. Loesel, R. M. Kurtz, C. Horvath, J. F. Bille, and G. Mourou, "Corneal refractive surgery with femtosecond lasers," IEEE J. Sel. Top. Quantum Electron. **5**, 902–910 (1999).
6. E. Klaseboer, S. W. Fong, C. K. Turangan, B. C. Khoo, A. J. Szeri, and M. L. Calvisi, "Interaction of lithotripter shockwaves with single inertial cavitation bubbles," J. Fluid Mech. **593**, 33–56 (2007).
7. A. A. Oraevsky, L. B. Da Silva, A. M. Rubenchik, M. D. Feit, M. E. Glinsky, and M. D. Perry, "Plasma mediated ablation of biological tissues with nanosecond-to-femtosecond laser pulses: Relative role of linear and nonlinear absorption," IEEE J. Sel. Top. Quantum Electron. **2**, 801–809 (1996).
8. A. Vogel and V. Venugopalan, "Mechanisms of pulsed laser ablation of biological tissues," Chem. Rev. **103**, 577–644 (2003).
9. E. A. Brujan, T. Ikeda, K. Yoshinaka, and Y. Matsumoto, "The final stage of the collapse of a cloud of bubbles close to a rigid boundary," Ultrason. Sonochem. **18**, 59–64 (2011).
10. F. Docchio, P. Regondi, M. R. Capon, and J. Mellerio, "Study of the temporal and spatial dynamics of plasmas induced in liquids by nanosecond Nd:YAG laser pulses. 1: Analysis of the plasma starting times," Appl. Opt. **27**, 3661–3668 (1988).
11. O. Baghdassarian, B. Tabbert, and G. Williams, "Luminescence characteristics of laser-induced bubbles in water," Phys. Rev. Lett. **83**, 2437–2440 (1999).
12. J. Noack and A. Vogel, "Single-shot spatially resolved characterization of laser-induced shock waves in water," Appl. Opt. **37**, 4092–4099 (1998).
13. W. Lauterborn and C. D. Ohl, "Cavitation bubble dynamics," Ultrason. Sonochem. **4**, 65–75 (1997).
14. B. C. Stuart, M. D. Feit, S. Herman, A. M. Rubenchik, B. W. Shore, and M. D. Perry, "Optical ablation by high-power short-pulse lasers," J. Opt. Soc. Am. B **13**, 459–468 (1996).
15. F. G. Pérez-Gutiérrez, S. Camacho-López, and G. Aguilar, "Time-resolved study of the mechanical response of tissue phantoms to nanosecond laser pulses," J. Biomed. Opt. **16**, 115001 (2011).
16. P. Gregorčič, "Measurements of cavitation bubble dynamics based on a beam-deflection probe," Appl. Phys. A, **93**, 901–905 (2008).
17. R. Petkovsek, P. Gregorcic, and J. Mozina, "A beam-deflection probe as a method for optodynamic measurements of cavitation bubble oscillations," Meas. Sci. Technol. **18**, 2972–2978 (2007).
18. L. F. Devia-Cruz, F. G. Pérez-Gutiérrez, and D. García-Casillas, "High resolution optical experimental technique for computing pulsed laser-induced cavitation bubble dynamics in a single shot," Atomization Sprays **23**, 505–515 (2013).
19. P. Prentice, A. Cuschieri, K. Dholakia, M. Prausnitz, and P. Campbell, "Membrane disruption by optically controlled microbubble cavitation," Nat. Phys. **1**, 107–110 (2005).
20. L. F. Devia-Cruz, S. Camacho-López, R. Evans, D. García-Casillas, and S. Stepanov, "Laser-induced cavitation phenomenon studied using three different optically-based approaches—An initial overview of results," Photon. Lasers Med. **1**, 1–11 (2012).
21. J. W. Goodman, *Introduction to Fourier Optics* (McGraw-Hill, 1968).
22. P. Schiebener, J. Straub, J. M. H. Levelt Sengers, and J. S. Gallagher, "Refractive index of water and steam as function of wavelength, temperature and density," J. Phys. Chem. Ref. Data **19**, 677 (1990).
23. R. Evans and S. Camacho-López, "Pump-probe imaging of nanosecond laser-induced bubbles in distilled water solutions: Observations of laser-produced-plasma," J. Appl. Phys. **108**, 103106 (2010).
24. I. Akhatov, O. Lindau, A. Topolnikov, R. Mettin, N. Vakhitova, and W. Lauterborn, "Collapse and rebound of a laser-induced cavitation bubble," Phys. Fluids **13**, 2805 (2001).